PHYSICAL REVIEW B **109**, L081106 (2024)

Letter

Ubiquitous nematic Dirac semimetal emerging from interacting quadratic band touching systems

Hongyu Lu,[1] Kai Sun,[2,*] Zi Yang Meng,[1,†] and Bin-Bin Chen[1,‡]
[1]*Department of Physics and HKU-UCAS Joint Institute of Theoretical and Computational Physics, The University of Hong Kong, Pokfulam Road, Hong Kong SAR, China*
[2]*Department of Physics, University of Michigan, Ann Arbor, Michigan 48109, USA*

(Received 1 June 2023; revised 19 August 2023; accepted 23 January 2024; published 12 February 2024)

Quadratic band touching (QBT) points are widely observed in two- and three-dimensional (2D and 3D) materials, including bilayer graphene and Luttinger semimetals, and attract significant attention from theory to experiment. However, even in its simplest form, the 2D checkerboard lattice QBT model, the phase diagram characterized by temperature and interaction strength, still remains unknown beyond the weak-coupling regime. Intense debates persist regarding the existence of various interaction-driven insulating states in this system. To address these uncertainties, we employ thermal tensor network simulations, specifically exponential tensor renormalization group and tangent space tensor renormalization group, along with density matrix renormalization group calculations to provide a comprehensive finite-temperature phase diagram for this model and shed light on previous ambiguities. Notably, our findings reveal the emergence of a robust bond-nematic Dirac semimetal phase with distinct thermodynamic properties that set it part from the nematic insulating state and other symmetry-broken states. This previously overlooked feature is found to be ubiquitous in interacting QBT systems. We also discuss the implications of these results for experimental systems such as bilayer graphene and iridate compounds.

DOI: 10.1103/PhysRevB.109.L081106

Introduction. Quadratic band touching (QBT) points are widely observed in materials. In the two-dimensional (2D) realm, bilayer graphene serves as a representative example [1–5], while in 3D, materials such as α-Sn, HgTe, and pyrochlore iridates $R_2Ir_2O_7$ ($R =$ Pr, Nd) exhibit Luttinger semimetal behavior [6–14]. Investigating the effects of interactions on QBTs is both fundamentally significant and experimentally relevant. For instance, understanding how QBTs transform into symmetry-breaking phases in bilayer graphene under the influence of trigonal warping and Coulomb interactions, or how Luttinger semimetals can evolve into Dirac, nodal-line, or Weyl semimetals, and even non-Fermi-liquid states in the presence of strain, bulk-inversion asymmetry, and Coulomb interactions, remains an active area of intense theoretical and experimental investigations [1–5,7–14].

The 2D checkerboard lattice model with C_4 symmetry serves as the simplest platform to investigate the effects of interactions on QBT points. Previous studies have revealed that a quantum anomalous Hall (QAH) state with spontaneously broken time-reversal symmetry (TRS) [15–30] emerges in the weak-coupling regime [31–36]. Proposals have also been put forth to realize QBT and interaction-driven QAH states in real materials, which include the four-band checkerboard lattice system based on monolayer $CrCl_2$(pyrazine)$_2$ [37], as well as the C_6 symmetric kagome metals [38–43].

Beyond the weak-coupling regime, the QAH phase is anticipated to give way to other competing phases, such as the C_2 symmetric site-nematic insulator (SNI) [31]. However, due to the strong-coupling nature of these phases, a complete phase diagram remains a subject of debate, with conflicting results [31–37]. Exact diagonalization (ED) and density matrix renormalization group (DMRG) simulations suggest that there is no coexisting region between the QAH and SNI states [33]. Instead, a C_4 symmetry-breaking bond-nematic Dirac semimetal (BNDS) phase emerges as an intermediate phase, where the QBT splits into two Dirac cones [35]. Notably, the BNDS and SNI were identified as distinct thermodynamic phases with different order parameters [35].

The transitions between QAH, BNDS, and SNI phases are found to be first order, different from the interaction-driven phase transitions in Bernal stacking graphene [2–5]. The previous studies [31–33,35] considered only nearest-neighbor (NN) interactions without next-nearest-neighbor (NNN) interactions, which are crucial for understanding the transition to other interaction-driven states such as the stripelike charge density wave insulator (referred to as stripe). Furthermore, the relationship between the BNDS and SNI phases has not been adequately addressed, and we demonstrate that they break exactly the same symmetry.

By incorporating NNN interactions into the system, Ref. [34] observed a direct transition from QAH or stripe to the SNI phase, omitting the BNDS phase. In a Hartree-Fock study of a doubled four-band checkerboard lattice [37], the BNDS phase was not reported. Instead, they discovered a Dirac semimetal phase with site-nematic order between the site-nematic insulator and the QBT semimetal. These

---

[*] sunkai@umich.edu
[†] zymeng@hku.hk
[‡] bchenhku@hku.hk

discrepancies highlight the ongoing challenges in achieving a consensus on the ground-state phase diagram of the checkerboard lattice QBT system. Furthermore, the finite-temperature phase diagram, especially the distinct $c_V \sim T^2$ behavior from emergent Dirac cones of the interaction-driven BNDS phase, needs to be explored.

In this Letter, by employing the exponential and tangent space tensor renormalization groups (XTRG and tanTRG) [44,45] and DMRG calculations, we unveil a comprehensive phase diagram based on thermodynamic characteristics. One key finding is the ubiquitous presence of the BNDS phase, which separates not only the QAH and SNI phases, but also the stripe and SNI phases. We clarify the equivalence of SNI and BNDS in terms of symmetry and reveal their distinct measurable properties, especially in their different thermodynamic properties. We foresee this overlooked interaction-driven BNDS with emergent Lorentz symmetry and unique thermodynamic properties could be a universal feature in interacting QBT systems, extending beyond the checkerboard lattice, with potential realizations in bilayer graphene [2–5], α-Sn, HgTe, and iridate compounds [6–14].

Model, method, and ground-state phase diagram. We examine a spinless fermion model in a checkerboard lattice,

$$\begin{aligned} H = \sum_{\mathbf{r}} \Bigg[& t \sum_{\gamma} c^{\dagger}_{\mathbf{r},B} c_{\mathbf{r}+\gamma,A} + \text{H.c.} \quad (\text{NN}) \\ & + t' \sum_{\lambda,i} (\eta_\lambda \epsilon_i) c^{\dagger}_{\mathbf{r},\lambda} c_{\mathbf{r}+\mathbf{a_i},\lambda} + \text{H.c.} \quad (\text{NNN}) \\ & + V_1 \sum_{\gamma} \left(n_{\mathbf{r},B} - \frac{1}{2}\right)\left(n_{\mathbf{r}+\gamma,A} - \frac{1}{2}\right) \quad (\text{NN}) \\ & + V_2 \sum_{\lambda,i} \left(n_{\mathbf{r},\lambda} - \frac{1}{2}\right)\left(n_{\mathbf{r}+\mathbf{a_i},\lambda} - \frac{1}{2}\right) \Bigg] \quad (\text{NNN}), \end{aligned} \tag{1}$$

with $\gamma \in \{\mathbf{0}, \mathbf{a_1}, \mathbf{a_2}, \mathbf{a_1}+\mathbf{a_2}\}$, $\lambda \in \{A, B\}$ being the sublattice index, $\{\eta_A = 1, \eta_B = -1\}$, and $\{\epsilon_1 = 1, \epsilon_2 = -1\}$, as shown in Fig. 1(a). We fix $t = -1$ and $t' = -0.5$ and consider both the repulsive NN and NNN density-density interactions.

We mainly employ the XTRG and tanTRG method [44–46] for finite-temperature simulations [27,46–50] with YC4×16 geometry and we retain up to $D = 1000$ bond states, rendering the truncation errors $\delta < 10^{-4}$ down to the low-T regime. We also perform YC6 DMRG simulations, with up to 4096 bond states and maximal truncation errors $\delta \approx 10^{-5}$.

Here, we set $V_1 = 4$ and systematically vary V_2 to demonstrate the existence of the BNDS phase between the QAH and SNI states. Additional numerical evidence supporting the presence of BNDS phases for different V_1 can be found in the Supplemental Material (SM) [51]. Furthermore, we investigate the large-interaction regime by fixing $V_1 = 6$ and varying V_2, revealing the occurrence of the BNDS phase between the stripe and SNI phases. The BNDS state is unambiguously characterized from both the low-T power-law behavior of specific heat ($c_V \sim T^2$), and the changes of conformal central charge c and the single-particle excitation gap via flux insertion. Consequently, we construct a comprehensive ground-state phase diagram, as illustrated in Fig. 1(b). Additionally, through comparing the symmetry of the two nematic states, BNDS and SNI, we find both states break exactly the same symmetry. In other words, akin to the gas-liquid and/or Lifshitz transitions, the first-order phase boundary between them does not involve a change in symmetry.

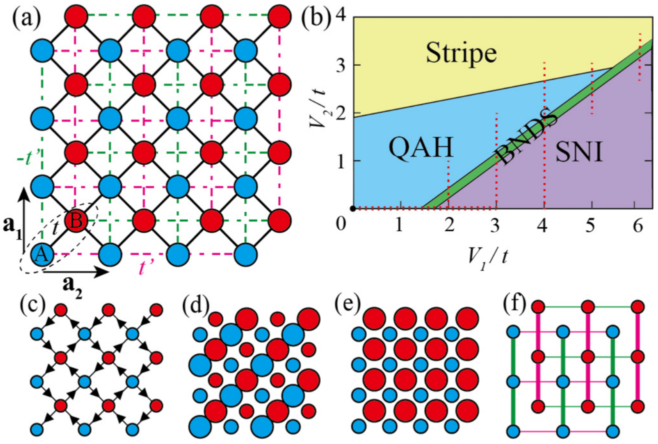

FIG. 1. (a) The checkerboard lattice with blue (red) dots denoting the A (B) sublattices. (b) The comprehensive ground-state phase diagram. The QBT is denoted by the black dot at the origin, while the red dotted lines represent the paths of simulations. (c)–(f) The real-space signature of the QAH, stripe, SNI, and BNDS phases, respectively. The QAH phase is depicted with arrows indicating the loop currents. In the stripe and SNI phases, large (small) dots represent high (low) electron density. In the BNDS phase, the thickness of the bonds corresponds to the absolute value of the hopping amplitude.

It is possible to establish an adiabatic pathway between these two states through exploring a higher-dimensional phase space. Regarding the bond- and site-nematic order parameters, without fine tuning, both of these order parameters remain nonzero in both the BNDS and SNI phases, reflecting their identical symmetry. This finding contrasts with the numerical results obtained from finite-size extrapolation as reported in previous work [35].

T-V phase diagram and the thermodynamic characteristics. To identify different phases in the T-V phase diagram, we utilize several measurements: *the* QAH structure factor $\mathcal{J}_{\text{QAH}} \equiv \frac{1}{N_b}\sum_{\langle i,j\rangle} \epsilon_{i,j} \langle \mathcal{C}_{ij}\mathcal{C}_{i_0 j_0}\rangle$, where the summation is over NN bonds in the bulk with N_b being the total number of bonds and $\epsilon_{i,j} = \pm 1$ characterizing the orientation of the current $\mathcal{C}_{ij} \equiv (c_i^{\dagger} c_j - c_j^{\dagger} c_i)$; the bond-nematic order parameter $\Delta_{\text{bond}} \equiv |\langle c^{\dagger}_{\mathbf{r},\lambda} c_{\mathbf{r}+\mathbf{a_2},\lambda}\rangle| - |\langle c^{\dagger}_{\mathbf{r},\lambda} c_{\mathbf{r}+\mathbf{a_1},\lambda}\rangle|$, which measures the difference in NNN hopping amplitudes along the vertical ($\mathbf{a}_2$) and horizontal ($\mathbf{a}_1$) directions; the site-nematic order parameter $\delta_{\text{site}} \equiv \langle n_{\text{B}} - n_{\text{A}}\rangle$, which quantifies the difference of the electron density at the "A" and "B" sublattices; the structure factor for the stripe phase $\mathcal{S}_{\text{stripe}} \equiv \frac{1}{N}\sum_i e^{-i\vec{k}\cdot\vec{r}_{0,i}} (\langle \hat{n}_i \hat{n}_0\rangle - \langle \hat{n}_i\rangle\langle \hat{n}_0\rangle)$, where $\vec{k} = (\pm\frac{\sqrt{2}\pi}{2}, \mp\frac{\sqrt{2}\pi}{2})$ represents the stripe pattern shown in Fig. 1(d); and the specific heat $c_V(T) \equiv \frac{\partial E(T)}{\partial T}$, where E is the energy density.

In Figs. 2(a)–2(d), we present various order parameters and structure factors, respectively. At $V_1 = 4$, when V_2 is small

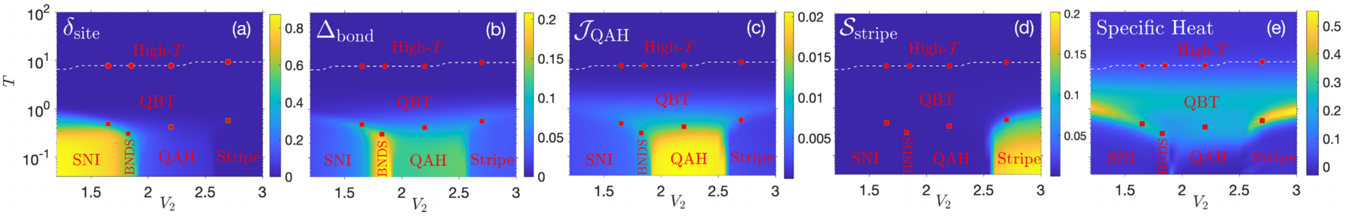

FIG. 2. The T-V_2 phase diagrams at $V_1 = 4$. Plots show (a) the SNI order parameter, (b) BNDS order parameter, (c) QAH structure factor, (d) stripe structure factor, and (e) specific heat c_V. The white dashed lines indicate the boundaries between the high-temperature thermal metallic regime and the intermediate-temperature QBT regime, identified using the red circles, which represent the crossover temperature between the high-T and QBT regimes, as illustrated in Figs. 3(a1)–3(d1). The red squares denote the transition temperature between the QBT regime to the low-temperature symmetry-breaking phases.

[Fig. 2(a)], the ground state is a SNI, and the order parameter $\delta_{\rm site}$, as well as the transition temperature, reduces as V_2 increases. In Fig. 2(b), an intermediate BNDS phase between QAH and SNI is clearly observed. This phase exhibits a strong bond-nematic order $\Delta_{\rm bond}$ Notably, the site-nematic order $\delta_{\rm site}$ is also present in the BNDS region and becomes stronger as V_2 decreases, ultimately exhibiting a significant jump across the phase boundary to the SNI phase. Furthermore, a sharp change in the QAH [Fig. 2(c)] and stripe [Fig. 2(d)] structure factors near the phase boundary $V_2 \sim 2.6$ indicates a first-order transition between these two phases. The specific heat shown in Fig. 2(e) also supports the identification of these phases with distinct characteristics.

To analyze the detailed thermodynamic transitions and features, we present four cuts of the 2D phase diagrams in Fig. 3. These cuts are taken along the temperature axis at fixed interactions, corresponding to four different ground states. At high temperatures (much larger than the bandwidth), the specific heat exhibits a scaling behavior of $c_V \sim T^{-2}$ for all cases. A crossover temperature can be identified where c_V deviates from the T^{-2} scaling, below which c_V displays two peaks or shoulders. The lower-temperature one marks the transition to the low-T ground state, which agrees with the order parameters/structure factors versus temperature, while the higher-temperature peak/shoulder is a thermodynamic characteristic of the electron band structure. With the latest tanTRG method, we are capable of fitting the low-T behavior of c_V, which has the exponential activation of $c_V \sim \exp(-\Delta/T)$ in the QAH, SNT, and stripe phases. More importantly, we can see the T^2 behavior of low-T c_V in the BNDS phase, which is the expected behavior of 2D Dirac cones and further supports that the BNDS phase is actually a Dirac semimetal, emerging from interaction-driven QBT systems.

We note that for the thermodynamics of the QAH state, at $V_1 = 4$, both its transition temperature and the amplitude of the loop current exhibit little dependence on V_2, as illustrated in Fig. 2(c) and SM [51]. In contrast, when V_2 is set to zero, the transition temperature and the amplitude of the loop current of the QAH state exhibit a strong dependence on V_1. As V_1 increases, both these two quantities increase before saturating at certain constant values. In addition, we add the DMRG results of the QAH order parameters to SM [51] for more evidence of the QAH state, which agrees with the finite-temperature phase diagram.

More importantly, with larger interactions, the QAH phase disappears, but the BNDS always survives as an intermediate phase between SNI and stripe, in direct contrast to the predictions from previous studies. The color figures in

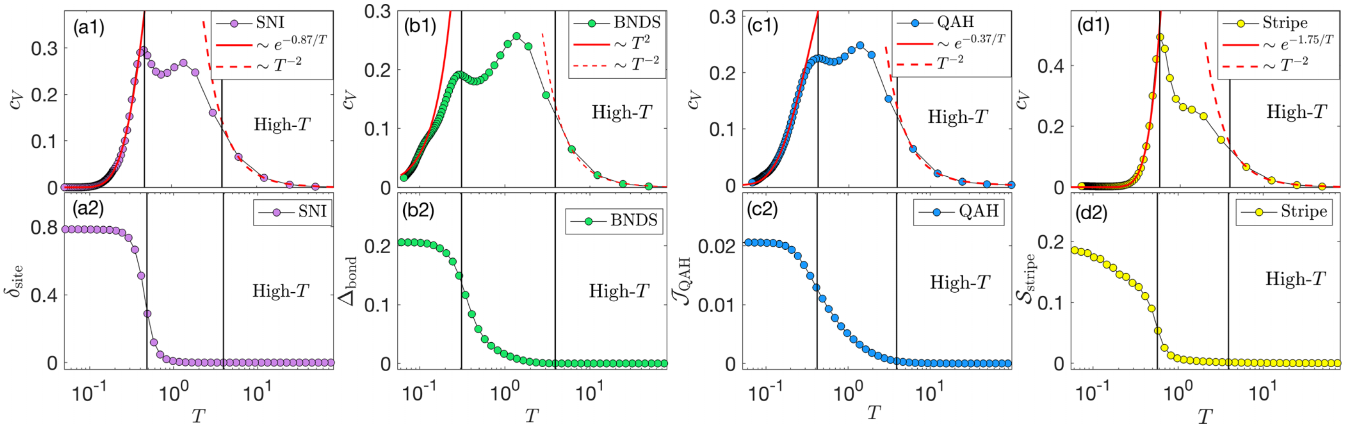

FIG. 3. The thermodynamic characteristics along the cuts in Fig. 2 as a function of temperature T. With fixed $V_1 = 4$, (a1) and (a2) represent SNI at $V_2 = 1.65$, (b1) and (b2) represent BNDS at $V_2 = 1.85$, (c1) and (c2) represent QAH at $V_2 = 2.2$, and (d1) and (d2) represent stripe at $V_2 = 2.7$. The first row displays the specific heat, while the second row shows the order parameters or structure factors for each phase. The separation temperature between the low-, intermediate-, and high-temperature regimes is indicated by the black solid lines. The $c_V \sim T^2$ for BNDS at low temperature is distinctively different from the $c_V \sim \exp(-\Delta/T)$ for the three other phases.

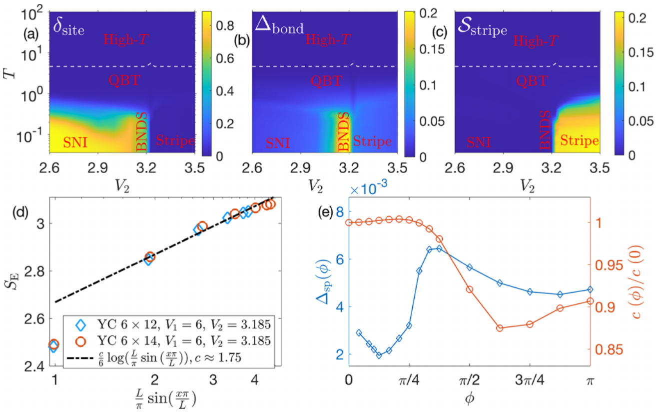

FIG. 4. The T-V_2 phase diagram with $V_1 = 6$, including (a) the site-nematic order, (b) the NNN bond-nematic order, and (c) the structure factor for stripe. (d) Entanglement entropy in the BNDS phase, with a log-scale horizontal axis. (e) With twisted boundary conditions in BNDS, by inserting flux ϕ, the single-particle gap and fitted central charge compared with that of no flux are shown. The corresponding shift of momenta grids is ϕ/L_y.

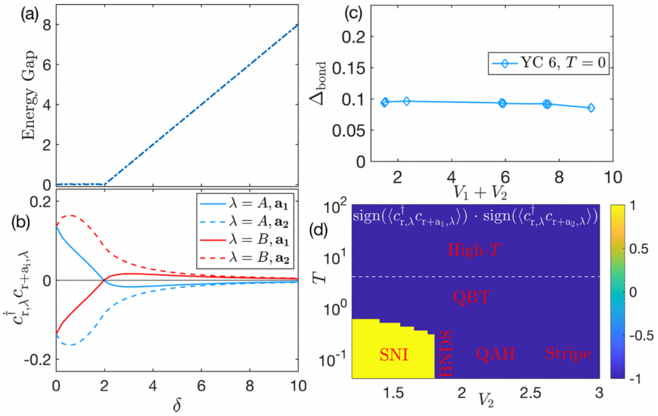

FIG. 5. (a), (b) Mean-field analysis. With increasing site-nematic order δ, the opening of the energy gap is shown in (a) and expectation values of NNN hoppings along the $\mathbf{a}_1$ ($\mathbf{a}_2$) directions for two sublattices respectively are shown in (b). (c) DMRG results of the NNN bond order of the BNDS phase throughout the phase diagram. (d) The product of signs of NNN hoppings along two directions with fixed $V_1 = 4$, which is ±1 if the hoppings take the same (opposite) sign(s).

Figs. 4(a)–4(c) clearly depict the stripe-BNDS-SNI transition, with fixed $V_1 = 6$ and varying V_2. To further verify the presence of the intermediate BNDS phase, we perform DMRG simulations within the BNDS phase and extract the conformal central charge from the entanglement entropy. By fitting the entanglement entropy as a function of the cylinder length to the universal scaling function $S_{\rm E}(x) = \frac{c}{6}\log(\frac{L}{\pi}\sin\frac{x\pi}{L})$, we obtain a central charge $c \approx 1.75$ with $D = 4096$ (which is still far from convergence), as shown in Fig. 4(d) and SM [51], which directly supports the existence of Dirac cones with emergent Lorentz symmetry in the BNDS phase. To further check the location of Dirac cones, we implement the twisted boundary conditions in the $\hat{y}$ direction by inserting the flux, $c_i^\dagger c_j + \text{H.c.} \to c_i^\dagger c_j e^{i\phi} + \text{H.c.}$, for all hopping terms across the boundary. For the same parameters in the BNDS phase, with $V_1 = 6$ and $V_2 = 3.185$, we fit the central charge c with certain flux ϕ, compared with that of no flux, and also measure the single-particle gap $\Delta_{\rm sp}(\phi)$ by extrapolating the ground-state energy at the half-filling sector and the lowest energy in the single-particle-excited sector (see details in SM [51]). As shown in Fig. 4(e), it is clear that the positions of Dirac cone are close to $(\pi, \pi \pm \pi/3)$ with a minute shift approximated $\phi/L_y \pm \pi/48$ (as denoted by the minimal of the single-particle gap, where the fitted central charge also saturates at its peak value), which is consistent with the mean-field analysis in the SM [51], and in this sense, the YC6 cylinder geometry is already close to be able to host the Dirac cones in the BNDS phase and our evidence of the Dirac cones is robust.

Furthermore, it is noteworthy that the strength of the NNN bond order in different regions of the BNDS phase remains almost constant around 0.1, as depicted in Fig. 5(c). Combining simulations at different V_1 and V_2, the phase diagram shown in Fig. 1(b) indicate that this BNDS arises universally as an intermediate phase between SNI and all other ground states in the phase space.

Mechanism of phase transition and nematic phases. We further perform a mean-field analysis to better understand the transitions and the bond- (site-) nematic phases. For the BNDS, we change the NNN hopping $t' \to (t' - \epsilon_i\Delta_{\rm bond})$ in Eq. (1) with positive $\Delta_{\rm bond}$; for the SNI, we add a sublattice chemical potential $\delta_{\rm site}\sum_{\mathbf{r}}(n_{\mathbf{r},A} - n_{\mathbf{r},B})$ to Eq. (1). At the quadratic level, a finite value of both $\delta_{\rm site}$ and $\Delta_{\rm bond}$ will split the QBT at (π, π) into two Dirac cones. From the perspective of symmetries, the QAH state breaks the TRS, while the BNDS and SNI states break the same lattice C_4 rotation symmetry into the same C_2 symmetry. In fact, our mean-field calculation (cf. SM [51]) shows that the site- (bond-) nematic term will also induce bond (site) order, which is consistent with our numerical results and clarifies the confusion in previous work [35], that the two nematic orders should be the same.

The difference between SNI and BNDS is not in symmetry but in their physical properties including the following: (1) With sufficiently strong site-nematic order $\delta_{\rm site}$, the two Dirac cones will merge and gap out as shown in Fig. 5(a), whereas the bond-nematic $\Delta_{\rm bond}$ term cannot gap out the Dirac cone; and (2) right after the gap-opening point, the sign structure of the NNN hopping amplitudes changes and the signs within the same sublattice become the same as shown in Fig. 5(b). We thus utilize such a feature to distinguish the SNI with the BNDS phase. Such as in the T-V phase diagram in Fig. 5(d), the sign structure of NNN hoppings clearly gives the SNI-BNDS boundary.

In our mean-field analysis, with the increase of $\delta_{\rm site}$, the two Dirac cones gradually merge into each other at the periodic boundary, and gap out the system, corresponding to the observed SNI. In reality, between the BNDS and SNI phases is an abrupt first-order transition, in that, although the two split Dirac cones move away from the (π, π) point, they cannot gradually merge into each other in the BNDS states but suddenly jump to the SNI state with a much larger $\delta_{\rm site}$ around the first-order transition, and the system is gapped out. Since there is no symmetry difference, the BNDS-SNI transition is similar to the liquid-gas transition, and one can in principle turn the first-order phase transition to an adiabatic crossover or a critical point through paths in higher-dimensional parameter space.

Discussions. In conclusion, we find the interaction-driven BNDS ubiquitously exists between SNI and the other interaction-driven insulating states in the checkerboard lattice QBT system, and we provide the complete ground-state and finite-temperature phase diagram with repulsive interactions, which solves the previous debates in this system [31–37]. We find the transition between BNDS and SNI in the phase diagram is similar to the liquid-gas transition and provide the numerical results of the thermodynamic characteristics, in that the BNDS state is characterized by $c_V \sim T^2$ of emergent Dirac cones from interacting QBT systems, distinctively different from the exponential form in other phases. The interaction-driven BNDS, with emergent Lorentz symmetry and unique thermodynamic properties, can stimulate a deeper understanding of the QBT systems and provide an alternative interaction-driven Dirac semimetal in materials such as kagome metals [38–43], bilayer graphene [2–5], and the α-Sn, HgTe, and iridate compound $R_2Ir_2O_7$ ($R =$ Pr, Nd) [10–12,14].

Acknowledgments. We thank W. Li and M. Scherer for discussions, and we in particular thank Lukas Janssen for the enlightening introduction of Luttinger semimetals and discussions on the interaction effect on QBT. H.Y.L. thanks Shou-Shu Gong for helpful discussions. H.Y.L., B.B.C., and Z.Y.M. acknowledge the support from the Research Grants Council (RGC) of Hong Kong Special Administrative Region of China (Project Nos. 17301721, AoE/P701/20, 17309822, C7037-22GF, 17302223), the ANR/RGC Joint Research Scheme sponsored by RGC of Hong Kong and French National Research Agency (Project No. A_HKU703/22). We thank the Beijng PARATERA Tech CO., Ltd. (URL https://cloud.paratera.com), the HPC2021 system under the Information Technology, The University of Hong Kong for providing HPC resources that have contributed to the research results reported within this paper.

---

[1] K. Yan, H. Peng, Y. Zhou, H. Li, and Z. Liu, Nano Lett. **11**, 1106 (2011).

[2] T. C. Lang, Z. Y. Meng, M. M. Scherer, S. Uebelacker, F. F. Assaad, A. Muramatsu, C. Honerkamp, and S. Wessel, Phys. Rev. Lett. **109**, 126402 (2012).

[3] S. Pujari, T. C. Lang, G. Murthy, and R. K. Kaul, Phys. Rev. Lett. **117**, 086404 (2016).

[4] S. Ray, M. Vojta, and L. Janssen, Phys. Rev. B **98**, 245128 (2018).

[5] S. Ray and L. Janssen, Phys. Rev. B **104**, 045101 (2021).

[6] J. M. Luttinger, Phys. Rev. **102**, 1030 (1956).

[7] E.-G. Moon, C. Xu, Y. B. Kim, and L. Balents, Phys. Rev. Lett. **111**, 206401 (2013).

[8] I. F. Herbut and L. Janssen, Phys. Rev. Lett. **113**, 106401 (2014).

[9] B. Cheng, T. Ohtsuki, D. Chaudhuri, S. Nakatsuji, M. Lippmaa, and N. P. Armitage, Nat. Commun. **8**, 2097 (2017).

[10] K. Wang, B. Xu, C. W. Rischau, N. Bachar, B. Michon, J. Teyssier, Y. Qiu, T. Ohtsuki, B. Cheng, N. P. Armitage, S. Nakatsuji, and D. van der Marel, Nat. Phys. **16**, 1194 (2020).

[11] T. Kondo, M. Nakayama, R. Chen, J. J. Ishikawa, E.-G. Moon, T. Yamamoto, Y. Ota, W. Malaeb, H. Kanai, Y. Nakashima *et al.*, Nat. Commun. **6**, 10042 (2015).

[12] L. Janssen and I. F. Herbut, Phys. Rev. B **95**, 075101 (2017).

[13] M. Kharitonov, J.-B. Mayer, and E. M. Hankiewicz, arXiv:2212.00902.

[14] I. Boettcher and I. F. Herbut, Phys. Rev. B **95**, 075149 (2017).

[15] D. J. Thouless, M. Kohmoto, M. P. Nightingale, and M. den Nijs, Phys. Rev. Lett. **49**, 405 (1982).

[16] K. von Klitzing, T. Chakraborty, P. Kim, V. Madhavan, X. Dai, J. McIver, Y. Tokura, L. Savary, D. Smirnova, A. M. Rey, C. Felser, J. Gooth, and X. Qi, Nat. Rev. Phys. **2**, 397 (2020).

[17] F. D. M. Haldane, Phys. Rev. Lett. **61**, 2015 (1988).

[18] C.-Z. Chang, J. Zhang, X. Feng, J. Shen, Z. Zhang, M. Guo, K. Li, Y. Ou, P. Wei, L.-L. Wang *et al.*, Science **340**, 167 (2013).

[19] Y. Deng, Y. Yu, M. Z. Shi, Z. Guo, Z. Xu, J. Wang, X. H. Chen, and Y. Zhang, Science **367**, 895 (2020).

[20] P. Stepanov, M. Xie, T. Taniguchi, K. Watanabe, X. Lu, A. H. MacDonald, B. A. Bernevig, and D. K. Efetov, Phys. Rev. Lett. **127**, 197701 (2021).

[21] F. D. M. Haldane, Phys. Rev. Lett. **93**, 206602 (2004).

[22] N. Nagaosa, J. Sinova, S. Onoda, A. H. MacDonald, and N. P. Ong, Rev. Mod. Phys. **82**, 1539 (2010).

[23] D. Xiao, M.-C. Chang, and Q. Niu, Rev. Mod. Phys. **82**, 1959 (2010).

[24] S. Raghu, X.-L. Qi, C. Honerkamp, and S.-C. Zhang, Phys. Rev. Lett. **100**, 156401 (2008).

[25] B.-B. Chen, Y. D. Liao, Z. Chen, O. Vafek, J. Kang, W. Li, and Z. Y. Meng, Nat. Commun. **12**, 5480 (2021).

[26] J. Liu and X. Dai, Phys. Rev. B **103**, 035427 (2021).

[27] X. Lin, B.-B. Chen, W. Li, Z. Y. Meng, and T. Shi, Phys. Rev. Lett. **128**, 157201 (2022).

[28] G. Pan, X. Zhang, H. Lu, H. Li, B.-B. Chen, K. Sun, and Z. Y. Meng, Phys. Rev. Lett. **130**, 016401 (2023).

[29] X. Zhang, G. Pan, B.-B. Chen, H. Li, K. Sun, and Z. Y. Meng, Phys. Rev. B **107**, L241105 (2023).

[30] C. Huang, X. Zhang, G. Pan, H. Li, K. Sun, X. Dai, and Z. Meng, arXiv:2304.14064.

[31] K. Sun, H. Yao, E. Fradkin, and S. A. Kivelson, Phys. Rev. Lett. **103**, 046811 (2009).

[32] S. Uebelacker and C. Honerkamp, Phys. Rev. B **84**, 205122 (2011).

[33] H.-Q. Wu, Y.-Y. He, C. Fang, Z. Y. Meng, and Z.-Y. Lu, Phys. Rev. Lett. **117**, 066403 (2016).

[34] S. Sur, S.-S. Gong, K. Yang, and O. Vafek, Phys. Rev. B **98**, 125144 (2018).

[35] T.-S. Zeng, W. Zhu, and D. Sheng, npj Quantum Mater. **3**, 49 (2018).

[36] H. Lu, S. Sur, S.-S. Gong, and D. N. Sheng, Phys. Rev. B **106**, 205105 (2022).

[37] X. Ji, J. Gao, C. Yue, Z. Wang, H. Wu, X. Dai, and H. Weng, Phys. Rev. B **106**, 235103 (2022).

[38] S. Nishimoto, M. Nakamura, A. O'Brien, and P. Fulde, Phys. Rev. Lett. **104**, 196401 (2010).

[39] J. Wen, A. Rüegg, C.-C. J. Wang, and G. A. Fiete, Phys. Rev. B **82**, 075125 (2010).

[40] W. Zhu, S.-S. Gong, T.-S. Zeng, L. Fu, and D. N. Sheng, Phys. Rev. Lett. **117**, 096402 (2016).

[41] H.-Y. Hui, M. Chen, S. Tewari, and V. W. Scarola, Phys. Rev. A **98**, 023609 (2018).

[42] S. Sankar, R. Liu, X.-J. Gao, Q.-F. Li, C. Chen, C.-P. Zhang, J. Zheng, Y.-H. Lin, K. Qian, R.-P. Yu, X. Zhang, Z. Y. Meng, K. Tuen Law, Q. Shao, and B. Jäck, arXiv:2303.03274.

[43] Y. Ren, T.-S. Zeng, W. Zhu, and D. N. Sheng, Phys. Rev. B **98**, 205146 (2018).

[44] B.-B. Chen, L. Chen, Z. Chen, W. Li, and A. Weichselbaum, Phys. Rev. X **8**, 031082 (2018).

[45] Q. Li, Y. Gao, Y.-Y. He, Y. Qi, B.-B. Chen, and W. Li, Phys. Rev. Lett. **130**, 226502 (2023).

[46] H. Li, B.-B. Chen, Z. Chen, J. von Delft, A. Weichselbaum, and W. Li, Phys. Rev. B **100**, 045110 (2019).

[47] L. Chen, D.-W. Qu, H. Li, B.-B. Chen, S.-S. Gong, J. von Delft, A. Weichselbaum, and W. Li, Phys. Rev. B **99**, 140404(R) (2019).

[48] H. Li, Y. D. Liao, B.-B. Chen, X.-T. Zeng, X.-L. Sheng, Y. Qi, Z. Y. Meng, and W. Li, Nat. Commun. **11**, 1111 (2020).

[49] B.-B. Chen, C. Chen, Z. Chen, J. Cui, Y. Zhai, A. Weichselbaum, J. von Delft, Z. Y. Meng, and W. Li, Phys. Rev. B **103**, L041107 (2021).

[50] D.-W. Qu, B.-B. Chen, X. Lu, Q. Li, Y. Qi, S.-S. Gong, W. Li, and G. Su, arXiv:2211.06322.

[51] See Supplemental Material at http://link.aps.org/supplemental/10.1103/PhysRevB.109.L081106 for the exponential tensor renormalization group and tangent space tensor renomalization group methods, the L scaling of the YC4 system at different phases, the T-V color figures at different regions of the ground-state phase diagram, the details of the determination of the high-T regime according the specific heat, the DMRG results of the QAH order parameter, the real-space loop pattern of the QAH state, the measurements of purified entanglement entropy, the details of DMRG results for fitting the central charge and measuring the single-particle gap with twisted boundary conditions in BNDS, and the mean-field analysis of the QBT, QAH, BNDS, and SNI phases.